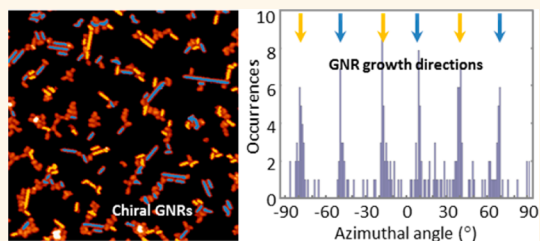# Bottom-Up Graphene-Nanoribbon Fabrication Reveals Chiral Edges and Enantioselectivity

Patrick Han,[†,‡,*] Kazuto Akagi,[†] Filippo Federici Canova,[†] Hirotaka Mutoh,[†] Susumu Shiraki,[†] Katsuya Iwaya,[§] Paul S. Weiss,[†,‡] Naoki Asao,[†,*] and Taro Hitosugi[†]

[†]Advanced Institute for Materials Research (AIMR), Tohoku University, Sendai, Miyagi 980-8577, Japan, [‡]California NanoSystems Institute and Departments of Chemistry and Biochemistry and Materials Science and Engineering, University of California, Los Angeles, Los Angeles, California 90095, United States, and [§]RIKEN Center for Emergent Matter Science (CEMS), Wako, Saitama 351-0198, Japan

ABSTRACT We produce precise chiral-edge graphene nanoribbons on Cu{111} using self-assembly and surface-directed chemical reactions. We show that, using specific properties of the substrate, we can change the edge conformation of the nanoribbons, segregate their adsorption chiralities, and restrict their growth directions at low surface coverage. By elucidating the molecular-assembly mechanism, we demonstrate that our method constitutes an alternative bottom-up strategy toward synthesizing defect-free zigzag-edge graphene nanoribbons.

KEYWORDS: graphene nanoribbons · surface-assisted molecular assembly · bottom-up fabrication · scanning tunneling microscopy

Graphene has extraordinary atomic and electronic structures.[1−3] To harness graphene's electronic[4] and magnetic properties,[5] one must first control the fabrication of graphene nanoribbons (GNRs) of desired widths and edge configurations.[3,6] The required degree of precision excludes conventional top-down fabrication processes, which inevitably introduce defects.[7−10] Surface-assisted molecular assembly (SAMA),[11−20] a bottom-up method, can produce defect-free armchair-edge GNRs of different widths,[21−23] but because current strategies rely entirely on precursor molecular structures to direct the assembly, to date, no one has synthesized a precursor that can yield different edge configurations. Here, we fabricate precise chiral-edge GNRs using SAMA that, besides molecular design, invoke a combination of distinct substrate properties to direct assembly. Specifically, we show that a precursor molecule, known to form armchair GNRs on inert surfaces *via* the Ullmann coupling reaction,[21] can be directed by a Cu{111} surface to undergo intermolecular cyclodehydrogenation (CDH) instead.[24] This particular combination of Cu surface properties enantioselectively distributes product chiral-edge (3,1)-GNRs along distinct azimuthal directions;

a phenomenon that enables asymmetric production of adsorbed chiral GNRs. We show that individual substrate properties can combine to override and/or to complement precursor molecular design, introducing new reaction pathways.

RESULTS AND DISCUSSION

We present our scanning tunneling microscopy (STM) measurements of (3,1)-GNR fabrication by thermally induced polymerization of 10,10′-dibromo-9,9′-bianthryl precursor monomers (DBPMs, structure in inset of Figure 1a) on Cu{111}. We interrogate the effects of annealing temperatures by performing three sets of experiments. All experiments start with DBPM deposition onto Cu{111} held at room temperature (RT) in ultrahigh vacuum. Subsequently, for each of the three sets of experiments, the sample was subjected to (i) no further annealing, (ii) 10 min annealing at 200 °C, and (iii) 10 min annealing at 500 °C, before STM imaging at T = 5.6 K. All STM images presented were recorded in topographic mode.
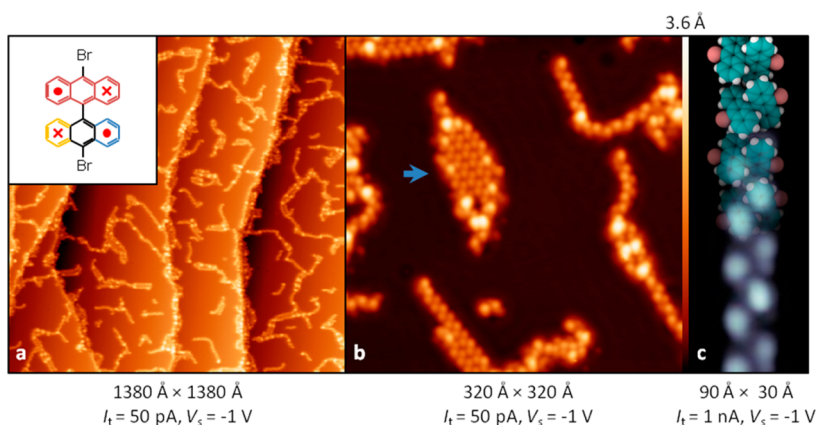
Figure 1 shows three STM images of Cu-{111} surface following DBPM deposition at RT (experiment (i)). Under these conditions, molecular chains (Figure 1a) are observed

3.6 Å

1380 Å × 1380 Å
I_t = 50 pA, V_s = -1 V

320 Å × 320 Å
I_t = 50 pA, V_s = -1 V

90 Å × 30 Å
I_t = 1 nA, V_s = -1 V

Figure 1. Self-assembled molecular chains. (a) Scanning tunneling microscope image of a Cu{111} surface after precursor deposition at room temperature. The inset of (a) shows the structure of 10,10′-dibromo-9,9′-bianthryl (DBPM). Dots (crosses) indicate regions away from (close to) the Cu substrate; pink lines highlight the region referred to as "anthryl unit"; yellow (blue) lines highlight regions referred to as "downward-pointing (upward-pointing) anthryl tips." (b) High-resolution STM image of a self-assembled DBPM chains and clusters. The blue arrow highlights a DBPM island. (c) Space-filling model of a DBPM chain overlapped with STM image. Carbon, hydrogen, and bromine atoms are represented by blue, white, and red spheres, respectively.

by STM as staggered protrusions (Figure 1b,c). The molecular chains exhibit long-range commensuration with Cu{111}, showing six preferential growth directions (Figure S1 in Supporting Information highlights two sets of 3-fold symmetries).

Because high-bias imaging of the observed molecular chains induces debromination (Supporting Information Figure S2), we deduce that the observed features are intact DBPMs self-assembled into chains. The staggered protrusions in Figure 1b,c are caused by the steric-hindrance-driven crossing of the bianthryl units within the DBPM molecules (dots and crosses in Figure 1a inset). Occasionally, two-dimensional (2D) DBPM islands are observed (blue arrow in Figure 1b). To investigate the structures of these chains and to understand the STM images, we used density functional theory (DFT) to model the adsorption of DBPM.

In Figure 2, we model a DBPM chain at 0 K, close to the imaging conditions of experiment (i). We calculated the ground-state adsorption configuration of a single DBPM (Figure 2a), determining the DBPM adsorption energy to be E_{ads} = 1.46 eV. We construct a bimolecular supercell with periodic boundary conditions by placing two ground-state DBPMs along the direction of the yellow dotted line in Figure 2b. This direction is 14° from the Cu{111} atomic rows (white dashed line in Figure 2b), and was chosen based on our STM azimuthal-angle measurements of GNRs (*vide infra*).
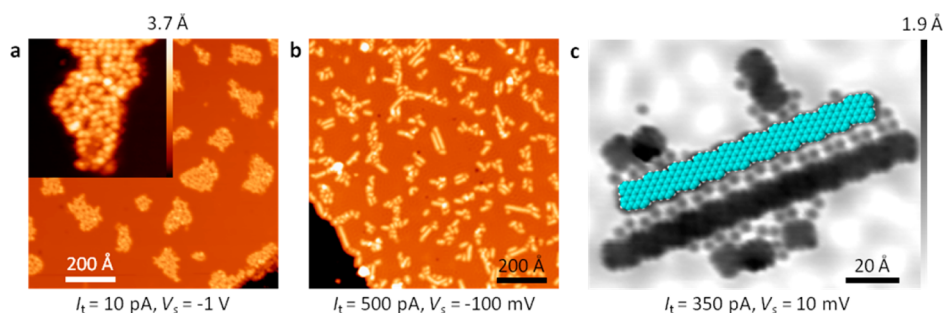
Figure 2b shows the relaxed configuration of the model DBPM chain. We found the molecules are stable in proximity with overlapping bianthryl tips. This overlap suggests the driving force for the DBPM chain formation stems from attractive π−π stacking interactions. We estimated the magnitude of interactions (E_{int}) between two DBPMs, using the scheme in Supporting Information Figure S3, yielding E_{int} = 0.115 eV.

E_{ads} = 1.46 eV

14°
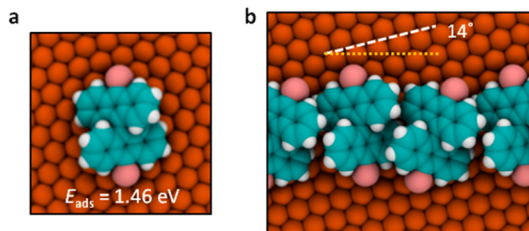
Figure 2. Intermolecular interactions between two DBPMs. (a) Ground-state adsorption configuration of a single DBPM. (b) Relaxed chain configuration of two DBPMs with periodic boundaries.

With these results we propose that at RT (*i.e.*, experiment (i)), π−π stacking interactions drive DBPM to form chain structures on Cu{111}, with an energy gain ΔE_{int} = 0.230 eV for a single molecule interacting with two neighbors (ΔE_{int} = 0.115 eV for molecules at chain extremities). Intermolecular Br−Br electrostatic repulsions may provide a barrier against 2D island formation observed in Figure 1b (Mulliken population at Br is calculated to be −0.13 e). Moreover, the DBPM azimuthal orientation with respect to the Cu{111} lattice depicted in Figure 2a is a feature of the ground-state DBPM adsorption, which explains the six preferred alignment directions of the DBPM chains observed in Supporting Information Figure S1 (*i.e.*, Figure 2a yields two mirror adsorption conformations, yielding two chain configurations per each of the three Cu{111}-atomic-row direction). In Figure 1c, we overlap the relaxed chain configuration (Figure 2b) with a DBPM chain imaged by STM.

Annealing the sample to 200 °C following RT DBPM deposition breaks up the chain structures observed in Figure 1 and induces DBPM island formation (experiment (ii), Figure 3a). The average apparent height of the islands in Figure 3a is comparable to that of the chain structures in Figure 1 (see Supporting Information

3.7 Å   1.9 Å

a   b   c

200 Å   200 Å   20 Å

$I_t = 10$ pA, $V_s = -1$ V $I_t = 500$ pA, $V_s = -100$ mV $I_t = 350$ pA, $V_s = 10$ mV

Figure 3. Thermally induced polymerization. (a) Scanning tunneling microscope image of a Cu{111} surface after DBPM deposition at RT, followed by 10 min thermal annealing of the surface at 200 °C. The inset shows a high-resolution STM image of a DBPM island. (b) Scanning tunneling microscope image of a Cu{111} surface after DBPM deposition at RT, followed by a 10 min thermal annealing of the surface at 500 °C. (c) Scanning tunneling microscope image of a chiral-edge GNR cluster. A space-filling model is superimposed over a 10-monomer-long GNR. The circular features in (c) were determined to be Br atoms.

Figure S4 for direct apparent-height comparison). As their internal structures suggests (Figure 3a inset), these islands are composed of many small 2D single-crystal DBPM domains (*e.g.*, blue arrow in Figure 1b). Because we image at $T = 5.6$ K, we cannot determine whether the observed islands are stable structures or are the quenched condensed phase of an equilibrium state with a 2D gas phase.[25]

Annealing the sample to 500 °C induces polymerization, yielding clusters of linear structures (experiment (iii), Figure 3b). High-resolution images reveal the characteristic chiral edge configuration of (3,1)-GNRs (Figure 3c). Both the size and the edge conformation of the overlaid space-filling model are consistent with the neighboring ribbons imaged by STM. The apparent height of the product is significantly lower compared to that of the unreacted molecules, indicating molecular flattening upon polymerization (Supporting Information Figure S4). The circular features in Figure 3c were determined to be free Br atoms by scanning tunneling spectroscopy (Supporting Information Figure S1c).[26]

The locations of the circular features in Figure 3c (*i.e.*, in between GNRs) indicate that these Br atoms were trapped immediately following debromination. This observation implies that debromination of DBPM occurs at $T_{deBr} > 200$ °C. This result is surprising, since Cu{111} is known to promote debromination of organic molecules even at RT.[26−31] We calculated the activation barrier for breaking a single DBPM C−Br bond on Cu{111} to be $E_{deBr} = 0.81$ eV (Figure S5). This suggests that at $T \leq 200$ °C, the time scale for thermal debromination of DBPM on Cu{111} is much longer compared to that of our sample manipulations (time between RT DBPM deposition on Cu{111} and sample introduction into 5.6 K environment is $t \leq 10$ min for experiment (i) and $t \leq 30$ min for experiment (ii)).

The trapped Br atoms also provide evidence that the GNR fabrication mechanism is not a diffusion-controlled process (*i.e.*, where molecular diffusion is the rate-limiting step of the assembly). Within the GNR cluster in Figure 3c, free Br atoms occupy all available space between ribbons, leaving edges without
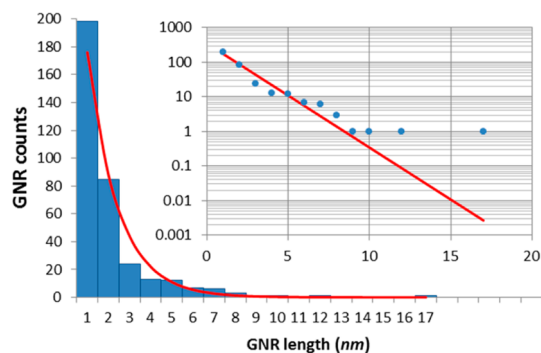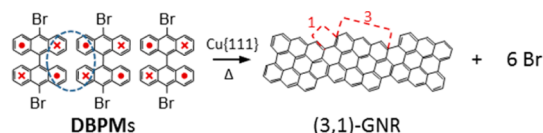

Figure 4. Length distribution of (3,1)-GNRs. The bar chart in the main panel shows the length distribution of 352 GNRs measured from Figure 5c. The GNR lengths are binned at 1 nm bin size. The red curve in the main panel shows the exponential decay $f(x) = (1/2)^x$. The inset displays the data from the main panel in the log scale. The count deviation for longer GNRs reflects the statistical limitations of single STM images.

neighboring GNRs devoid of Br atoms. This indicates that, for the observed cluster, polymerization occurred where DBPMs were already prepositioned for reaction at the polymerization onset. As GNRs are formed, Br atoms produced at the center of the cluster are trapped between ribbons, while Br atoms produced at the cluster edge are free to diffuse away.

The hypothesis that the current SAMA is not diffusion controlled is further supported by the GNR length distribution. The main panel in Figure 4 shows the length-distribution histogram compiled from the measurement of 352 ribbons from our STM images. This histogram indicates that the number of GNRs of the same length decays exponentially with GNR length (compare with $f(x) = (1/2)^x$, displayed as red curves in the same figure). This type of distribution is unusual compared to previous diffusion-controlled bottom-up GNR assemblies, which typically exhibit Γ-distribution in GNR lengths.[21,23] The fact that 198 out of 352 GNRs are 1 nm long (*i.e.*, one-DBPM long) is evidence that once polymerization starts, isolated and misaligned DBPMs can only undergo debromination and molecular flattening, without the possibility of subsequent diffusion or polymerization.

These results indicate that our product is a (3,1)-chiral-edge GNR formed by both Cu{111}-catalyzed debromination and Cu{111}-catalyzed CDH[24] between adjacent DBPMs (Figure 5). We propose that this polymerization can occur only in DBPM chains with configurations similar to those modeled in Figure 2b. We stress that Figure 2b illustrates the lowest energy arrangement and hence does not model a molecular configuration at high temperature. Instead, we postulate that, at high temperature, chains like those in Figure 2b are stabilized by a 2D condensed phase, prepositioning DBPMs for polymerization into (3,1)-GNRs.

Further, comparing our calculated $E_{deBr} = 0.81$ eV with the activation barrier calculated elsewhere for CDH, $E_{CDH} = 1.8$ eV,[24] we propose that DBPM polymerization on Cu{111} begins with debromination, followed by CDH. According to Figures 3c and 4, the debrominated DBPM radicals do not diffuse between the two reactions. Instead, they remain at the same
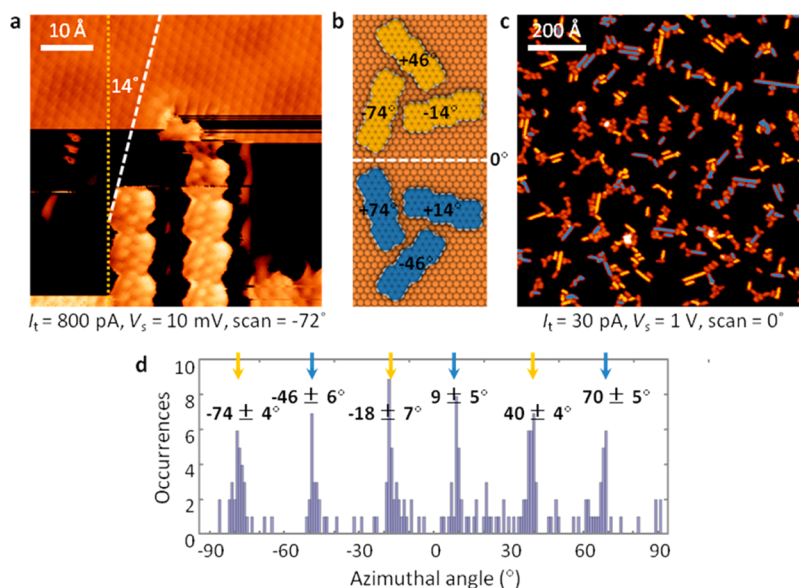
location where debromination occurs. For DBPM radicals that are prepositioned correctly, CDH ensues with the dehydrogenation of the downward-pointing anthryl tips (red crosses in Figure 5), triggering a cascade of CDH reactions in the region between DBPMs (blue dashed oval in Figure 5).[24] We visualize the polymerization mechanism as shown in the schematic in Supporting Information Figure S6.

Next, we demonstrate the Cu{111} surface structure is directly involved in the DBPM alignment into the chain configuration, conducive to polymerization. Figure 6a highlights the (3,1)-GNR commensuration with Cu{111} by partially resolving both structures through intermittent STM tip interactions with stray adsorbates.[32] As the white dashed line in Figure 6a indicates, the zigzag edges of the (3,1)-GNRs are aligned with one of the Cu{111} atomic row, indicating a 14° offset of the GNR axis (yellow dotted line) from the Cu atomic row direction.[33] The observed commensuration mode also entails six possible GNR growth directions: each of the three Cu{111} major axes, yielding two possible adsorption chiralities (depicted as yellow and blue mirror images in Figure 6b).

We tested the growth directions by digitally isolating GNRs in our STM images and by measuring their azimuthal angles with respect to the horizontal direction (see the Methods section for detail). In Figure 6c, we highlight the digitally isolated GNRs with lines colored according to the adsorption chiralities defined in Figure 6b. The adsorption chirality of each GNR was

Figure 5. Reaction scheme for the polymerization of DBPM into (3,1)-GNR. The red crosses (dots) indicate regions of the bianthryl units that are close to (away from) the Cu{111} substrate. The blue dashed oval highlights a region where cascade CDH reactions occur. The red dashed lines demonstrate the (3,1)-chiral edge nomenclature.

Figure 6. Graphene nanoribbons aligned by Cu{111}. (a) Scanning tunneling microscope image showing intermittent resolution of both (3,1)-GNR internal structures and Cu{111} surface atoms. The white dashed line shows the alignment of a (3,1)-GNR zigzag edge with a Cu{111} atomic row. The yellow dotted line shows the longitudinal axis of a (3,1)-GNR. (b) Models of the six possible (3,1)-GNR growth directions on Cu{111}. The bold numbers indicate the calculated azimuthal angle from the horizontal white dashed line, defined as 0°. Highlighting a Cu{111} atomic row, the white dashed line also represents an imaginary mirror line reflecting the "yellow" and "blue" adsorption chiralities. (c) Scanning tunneling microscope image of (3,1)-GNR clusters on Cu{111}. Blue and yellow lines mark individual ribbons selected digitally for the azimuthal-angle measurements and the measured adsorption chiralities as defined in (b). (d) Histogram showing the growth-direction distribution of (3,1)-GNRs in (c). Compare the measured angles with the calculated values in (b).

checked by STM (Supporting Information Figure S7). The angle measurements from all isolated GNRs are then compiled into the histogram in Figure 6d, showing six dominant growth directions, each of which composed of a single adsorption chirality (colored arrows in Figure 6d). This is consistent with both STM experiments (Supporting Information Figure S1) and DFT calculations, which predict six possible configurations of the unreacted DBPM chains on the Cu{111} lattice (Figure 2).

Next, we discuss the mechanism leading to the directionality of DBPM adsorption on Cu{111} (Figure 2a). To this end, we compare the single-DBPM E_{ads} calculated including van der Waals (vdW) interactions (E_{ads} = 1.46 eV) and excluding vdW interactions (E_{ads} = 0.09 eV, Supporting Information Figure S8). These results indicate that over 90% of the substrate-DBPM interactions are vdW in origin. From this, we propose that for the DBPM/Cu{111} system, vdW forces pull the molecules toward the surface forcing the molecular orbitals to interact with surface Cu atoms (Supporting Information Figure S8, main panel). This latter interaction enables preferential alignment of individual DBPMs with the Cu{111} atomic rows as depicted by the adsorption configurations in Figure 2. This preferential orientation dictates the direction of molecular chain formation as evidenced by Supporting Information Figure S1. The same interactions may also happen within the condensed island phase at high temperature, prepositioning DBPMs along the direction that is 14° from the Cu{111} atomic rows.

CONCLUSIONS AND PROSPECTS

We have demonstrated that the chemistries of SAMAs can be altered by specific properties of the substrate. The surface atomic structure of Cu{111} and its propensity to catalyze CDH combine to direct the DBPMs to polymerize into (3,1)-GNRs. Previous work on DBPM assemblies by Au{111} and Ag{111}[21] indicated that ideal substrates should be just reactive enough to lower the activation barriers of chemical reaction predetermined by the precursor molecular structure.[14,27,30,34,35] Our work shows that more reactive surfaces can be used to control the structure of the SAMA product, even dictating its symmetry. For example, the GNR-adsorption-chirality distribution is disperse over a Cu{111} terrace in Supporting Information Figure S9a. However, this dispersion is not retained on top of Cu{111} step edges. As Supporting Information Figure S9b shows, (3,1)-GNR growth occurs only over step-edge regions aligned with the preferred growth directions. This implies that, potentially, the (3,1)-GNR adsorption chirality can be selected by a vicinal Cu surface with high step density and controlled step directions, such as Cu{643},[36] opening possibilities for enantioselective heterogeneous catalysis. In the broader perspective of bottom-up fabrication, this work takes molecular assemblies out of the confine of weak interactions[12−14] to include processes involving covalent-bond manipulation. Previous STM work by Treier et al. showed Cu-catalyzed CDH as an intramolecular reaction where reacting entities are aligned and held in position by the covalent bonds of the molecules.[24] Our work demonstrates that the Cu substrate aligns multiple DBPMs and holds them with anthryl tips pointing at each other to form (3,1)-GNRs.[37,38] In the field of GNRs, our findings provide a strategy to design bottom-up methods of making precise GNRs of desired edge configuration, including the coveted zigzag edge.[5,7]

METHODS

Preparation and imaging of (3,1)-GNRs. The Cu{111} single crystal (MaTecK GmbH, Jülich, Germany) was prepared by repeated cycles of Ar$^+$ ion bombardment and annealing at 500 °C and cooled down to RT for use as substrate for GNR growth. 10,10′-Dibromo-9,9′-bianthryl precursor monomers (synthesized according to method reported in ref 21) were deposited in ultrahigh vacuum by sublimation using a custom-made Knudsen cell at RT. Polymerization was performed by annealing DBPM/Cu{111} at 500 °C for 10 min. Surface coverages were monitored by a custom-made STM.[39] All STM images were acquired at 5.6 K, and were processed with WSXM software.[40] We used W tips custom-etched from polycrystalline wires. We monitored our sample temperature optically using an infrared pyrometer. Our Cu sample (7 mm × 2 mm × 1 mm) is heated using a filament located at its backside.

Density Functional Theory. Our calculations were done using VASP code,[41] with PAW potentials and revised vdW-DF2 functional.[42] The single-molecule calculations were performed with a supercell of 1.536 nm × 1.773 nm × 2.353 nm, extended to 1.845 nm × 1.846 nm × 1.810 nm for simulations of the periodic chain. The molecular chains were constructed by repeating DBPM dimers along the direction 13.89° from the Cu{111} atomic row. The angle was chosen based on the product GNR alignment with Cu{111} observed by STM. In all cases, the supercells included three Cu atomic layers, and the atoms in the lowermost layer were fixed to their ideal positions. Structure optimizations were performed with E_{cutoff} of 400 eV and 2 × 2 × 1 Monkhorst–Pack k-points grid. The vdW contribution to all adsorption and interaction energies was obtained through comparison against PBE96 calculations.[43] Molecular dynamics simulations were performed considering only Γ-point, and an integration time step of 1.0 fs: hydrogen atoms were replaced by deuterium.

Angle-Measurements and Length-Distribution Image Processing. Scanning tunneling microscopy topographs were converted into gray scale images where pixel values range between 0 and 1. We applied the morphological components detection algorithm available in Wolfram Mathematica, with a threshold of 0.574. Fitting all detected features to ellipsoids provides an estimate of their size, elongation, and orientation. Small image features (area <28 pixels) were removed from all analysis as they could not be reliably fitted; for angle measurement, round features (elongation < 0.5) were ignored as well.

Conflict of Interest: The authors declare no competing financial interest.

Supporting Information Available: Additional figures showing DFT information on the energetics of the GNR fabrication process; additional figures showing STM information on reactant

apparent heights, byproduct identity, and global substrate effects. This material is available free of charge *via* the Internet at http://pubs.acs.org.

REFERENCES AND NOTES

1. Novoselov, K. S.; Fal'ko, V. I.; Colombo, L.; Gellert, P. R.; Schwab, M. G.; Kim, K. A Roadmap for Graphene. *Nature* **2012**, *490*, 192–200.
2. Yazyev, O. V. A Guide to the Design of Electronic Properties of Graphene Nanoribbons. *Acc. Chem. Res.* **2013**, *46*, 2319–2328.
3. Yazyev, O. V. Emergence of Magnetism in Graphene Materials and Nanostructures. *Rep. Prog. Phys.* **2010**, *73*, 056501.
4. Son, Y. W.; Cohen, M. L.; Louie, S. G. Energy Gaps in Graphene Nanoribbons. *Phys. Rev. Lett.* **2006**, *97*, 216803.
5. Son, Y. W.; Cohen, M. L.; Louie, S. G. Half-Metallic Graphene Nanoribbons. *Nature* **2006**, *444*, 347–349.
6. Prezzi, D.; Eom, D.; Rim, K. T.; Zhou, H.; Xiao, S.; Nuckolls, C.; Heinz, T. F.; Flynn, G. W.; Hybertsen, M. S. Edge Structures for Nanoscale Graphene Islands on Co(0001) Surfaces. *ACS Nano* **2014**, *8*, 5765–5773.
7. Yan, L.; Zheng, Y. B.; Zhao, F.; Li, S. J.; Gao, X. F.; Xu, B. Q.; Weiss, P. S.; Zhao, Y. L. Chemistry and Physics of a Single Atomic Layer: Strategies and Challenges for Functionalization of Graphene and Graphene-Based Materials. *Chem. Soc. Rev.* **2012**, *41*, 97–114.
8. Sprinkle, M.; Ruan, M.; Hu, Y.; Hankinson, J.; Rubio-Roy, M.; Zhang, B.; Wu, X.; Berger, C.; de Heer, W. A. Scalable Templated Growth of Graphene Nanoribbons on SiC. *Nat. Nanotechnol.* **2010**, *5*, 727–731.
9. Tao, C. G.; Jiao, L. Y.; Yazyev, O. V.; Chen, Y. C.; Feng, J. J.; Zhang, X. W.; Capaz, R. B.; Tour, J. M.; Zettl, A.; Louie, S. G.; *et al.* Spatially Resolving Edge States of Chiral Graphene Nanoribbons. *Nat. Phys.* **2011**, *7*, 616–620.
10. Martin-Fernandez, I.; Wang, D. B.; Zhang, Y. G. Direct Growth of Graphene Nanoribbons for Large-Scale Device Fabrication. *Nano Lett.* **2012**, *12*, 6175–6179.
11. Weiss, P. S.; Kamma, M. M.; Graham, T. M.; Stranick, S. J. Imaging Benzene Molecules and Phenyl Radicals on Cu{111}. *Langmuir* **1998**, *14*, 1284–1289.
12. Han, P.; Weiss, P. S. Electronic Substrate-Mediated Interactions. *Surf. Sci. Rep.* **2012**, *67*, 19–81.
13. Koepf, M.; Cherioux, F.; Wytko, J. A.; Weiss, J. 1D and 3D Surface-Assisted Self-Organization. *Coord. Chem. Rev.* **2012**, *256*, 2872–2892.
14. El Garah, M.; MacLeod, J. M.; Rosei, F. Covalently Bonded Networks through Surface-Confined Polymerization. *Surf. Sci.* **2013**, *613*, 6–14.
15. Adisoejoso, J.; Li, Y.; Liu, J.; Liu, P. N.; Lin, N. Two-Dimensional Metallo-supramolecular Polymerization: Toward Size-Controlled Multi-Strand Polymers. *J. Am. Chem. Soc.* **2012**, *134*, 18526–18529.
16. Lafferentz, L.; Eberhardt, V.; Dri, C.; Africh, C.; Comelli, G.; Esch, F.; Hecht, S.; Grill, L. Controlling On-Surface Polymerization by Hierarchical and Substrate-Directed Growth. *Nat. Chem.* **2012**, *4*, 215–220.
17. Arado, O. D.; Monig, H.; Wagner, H.; Franke, J. H.; Langewisch, G.; Held, P. A.; Studer, A.; Fuchs, H. On-Surface Azide-Alkyne Cycloaddition on Au(111). *ACS Nano* **2013**, *7*, 8509–8515.
18. Xu, L. R.; Zhou, X.; Yu, Y. X.; Tian, W. Q.; Ma, J.; Lei, S. B. Surface-Confined Crystalline Two-Dimensional Covalent Organic Frameworks *via* On-Surface Schiff-Base Coupling. *ACS Nano* **2013**, *7*, 8066–8073.
19. Fan, Q. T.; Wang, C. C.; Liu, L. M.; Han, Y.; Zhao, J.; Zhu, J. F.; Kuttner, J.; Hilt, G.; Gottfried, J. M. Covalent, Organometallic, and Halogen-Bonded Nanomeshes from Tetrabromo-Terphenyl by Surface-Assisted Synthesis on Cu(111). *J. Phys. Chem. C* **2014**, *118*, 13018–13025.
20. Müllen, K. Evolution of Graphene Molecules: Structural and Functional Complexity as Driving Forces behind Nanoscience. *ACS Nano* **2014**, *8*, 6531–6541.
21. Cai, J. M.; Ruffieux, P.; Jaafar, R.; Bieri, M.; Braun, T.; Blankenburg, S.; Muoth, M.; Seitsonen, A. P.; Saleh, M.; Feng, X. L.; *et al.* Atomically Precise Bottom-Up Fabrication of Graphene Nanoribbons. *Nature* **2010**, *466*, 470–473.
22. Chen, Y. C.; de Oteyza, D. G.; Pedramrazi, Z.; Chen, C.; Fischer, F. R.; Crommie, M. F. Tuning the Band Gap of Graphene Nanoribbons Synthesized from Molecular Precursors. *ACS Nano* **2013**, *7*, 6123–6128.
23. Linden, S.; Zhong, D.; Timmer, A.; Aghdassi, N.; Franke, J. H.; Zhang, H.; Feng, X.; Mullen, K.; Fuchs, H.; Chi, L.; *et al.* Electronic Structure of Spatially Aligned Graphene Nanoribbons on Au(788). *Phys. Rev. Lett.* **2012**, *108*, 216801.
24. Treier, M.; Pignedoli, C. A.; Laino, T.; Rieger, R.; Mullen, K.; Passerone, D.; Fasel, R. Surface-Assisted Cyclodehydrogenation Provides a Synthetic Route towards Easily Processable and Chemically Tailored Nanographenes. *Nat. Chem.* **2011**, *3*, 61–67.
25. Kulawik, M.; Rust, H. P.; Heyde, M.; Nilius, N.; Mantooth, B. A.; Weiss, P. S.; Freund, H. J. Interaction of CO Molecules with Surface State Electrons on Ag(111). *Surf. Sci.* **2005**, *590*, L253–L258.
26. Nanayakkara, S. U.; Sykes, E. C. H.; Fernandez-Torres, L. C.; Blake, M. M.; Weiss, P. S. Long-Range Electronic Interactions at a High Temperature: Bromine Adatom Islands on Cu(111). *Phys. Rev. Lett.* **2007**, *98*, 206108.
27. Koch, M.; Gille, M.; Viertel, A.; Hecht, S.; Grill, L. Substrate-Controlled Linking of Molecular Building Blocks: Au(111) *vs* Cu(111). *Surf. Sci.* **2014**, *627*, 70–74.
28. Gutzler, R.; Walch, H.; Eder, G.; Kloft, S.; Heckl, W. M.; Lackinger, M. Surface Mediated Synthesis of 2D Covalent Organic Frameworks: 1,3,5-Tris(4-bromophenyl)benzene on Graphite(001), Cu(111), and Ag(110). *Chem. Commun.* **2009**, 4456–4458.
29. Doyle, C. M.; Krasnikov, S. A.; Sergeeva, N. N.; Preobrajenski, A. B.; Vinogradov, N. A.; Sergeeva, Y. N.; Senge, M. O.; Cafolla, A. A. Evidence for the Formation of an Intermediate Complex in the Direct Metalation of Tetra(4-Bromophenyl)-Porphyrin on the Cu(111) Surface. *Chem. Commun.* **2011**, *47*, 12134–12136.
30. Di Giovannantonio, M.; El Garah, M.; Lipton-Duffin, J.; Meunier, V.; Cardenas, L.; Revurat, Y. F.; Cossaro, A.; Verdini, A.; Perepichka, D. F.; Rosei, F.; *et al.* Insight into Organometallic Intermediate and Its Evolution to Covalent Bonding in Surface-Confined Ullmann Polymerization. *ACS Nano* **2013**, *7*, 8190–8198.
31. Gutzler, R.; Cardenas, L.; Lipton-Duffin, J.; El Garah, M.; Dinca, L. E.; Szakacs, C. E.; Fu, C. Y.; Gallagher, M.; Vondracek, M.; Rybachuk, M.; *et al.* Ullmann-Type Coupling of Brominated Tetrathienoanthracene on Copper and Silver. *Nanoscale* **2014**, *6*, 2660–2668.
32. Han, P.; Mantooth, B. A.; Sykes, E. C. H.; Donhauser, Z. J.; Weiss, P. S. Benzene on Au {111} at 4 K: Monolayer Growth and Tip-Induced Molecular Cascades. *J. Am. Chem. Soc.* **2004**, *126*, 10787–10793.
33. Gao, L.; Guest, J. R.; Guisinger, N. P. Epitaxial Graphene on Cu(111). *Nano Lett.* **2010**, *10*, 3512–3516.
34. McCarty, G. S.; Weiss, P. S. Formation and Manipulation of Protopolymer Chains. *J. Am. Chem. Soc.* **2004**, *126*, 16772–16776.
35. Mendez, J.; Lopez, M. F.; Martin-Gago, J. A. On-Surface Synthesis of Cyclic Organic Molecules. *Chem. Soc. Rev.* **2011**, *40*, 4578–4590.
36. Baber, A. E.; Gellman, A. J.; Sholl, D. S.; Sykes, E. C. H. The Real Structure of Naturally Chiral Cu{643}. *J. Phys. Chem. C* **2008**, *112*, 11086–11089.

37. Leung, L.; Lim, T.; Ning, Z.; Polanyi, J. C. Localized Reaction at a Smooth Metal Surface: *p*-Diiodobenzene at Cu(110). *J. Am. Chem. Soc.* **2012**, *134*, 9320–9326.

38. Cheng, F.; Ji, W.; Leung, L.; Ning, Z.; Polanyi, J. C.; Wang, C.-G. How Adsorbate Alignment Leads to Selective Reaction. *ACS Nano* **2014**, *8*, 8669–8675.

39. Iwaya, K.; Shimizu, R.; Hashizume, T.; Hitosugi, T. Systematic Analyses of Vibration Noise of a Vibration Isolation System for High-Resolution Scanning Tunneling Microscopes. *Rev. Sci. Instrum.* **2011**, *82*, 083702.

40. Horcas, I.; Fernandez, R.; Gomez-Rodriguez, J. M.; Colchero, J.; Gomez-Herrero, J.; Baro, A. M. WSXM: A Software for Scanning Probe Microscopy and a Tool for Nanotechnology. *Rev. Sci. Instrum.* **2007**, *78*, 013705.

41. Kresse, G.; Furthmuller, J. Efficient Iterative Schemes for *ab Initio* Total-Energy Calculations Using a Plane-Wave Basis Set. *Phys. Rev. B* **1996**, *54*, 11169–11186.

42. Hamada, I. van der Waals Density Functional Made Accurate. *Phys. Rev. B* **2014**, *89*, 121103(R).

43. Perdew, J. P.; Burke, K.; Ernzerhof, M. Generalized Gradient Approximation Made Simple. *Phys. Rev. Lett.* **1996**, *77*, 3865–3868.